Received: 8 May 2021 | Revised: 3 October 2021 | Accepted: 18 November 2021

DOI: 10.1002/nag.3313

RESEARCH ARTICLE

WILEY

Laboratory and discrete-based numerical investigation on the collision problem of impactor-block systems with soft-porous and hard-crystalline analog rocks

Lina Luo[1] | **Sathwik S. Kasyap**[1] | **Huan He**[2] | **Kostas Senetakis**[1]

[1] Department of Architecture and Civil Engineering, City University of Hong Kong, Hong Kong, SAR, China

[2] Institute of Geotechnical Engineering, Southeast University, Nanjing, China

Correspondence
Kostas Senetakis, Department of Architecture and Civil Engineering, City University of Hong Kong, Hong Kong, SAR China.
Email: ksenetak@cityu.edu.hk

Funding information
Research Grants Council of the Hong Kong Special Administrative Region, China, Grant/Award Numbers: CityU 11210419, CityU 11214218

Abstract

We investigated experimentally the normal coefficient of restitution (COR) of impactors colliding on the surfaces of two different blocks; a soft-porous block composed of plaster (dry impacts) and a hard-crystalline rock composed of granite (dry and wet impacts). The experiments were performed in a range of low-impact velocities and various particle types were used including perfectly spherical smooth glass beads and ceramic balls, rough glass beads as well as natural rough sand grains. Image processing was carried out to quantify the formed contours of craters caused by the surface damage of the soft blocks due to the impact. The results indicated very low COR values on the plaster block compared with the granite block as the energy was dissipated by means of surface plastic deformations on the plaster, however the contour crater images showed that the collision mechanisms depended on the roughness of the impactor. The behavior of impactor-fluid-block systems was dependent on both surface roughness and global morphology of the impactors. Discrete-based (DEM) numerical simulations were performed to provide further insights into the behavior of the impactor-block systems subjected to collision using the COR values from the experiments as the micro-scale parameters and data from the literature as the macro-scale parameters for the model calibration. The numerical output was used to observe the development of compression and tension force chain networks and how these involved during and after impact on different base blocks.

KEYWORDS
coefficient of restitution, collision, DEM, force chain network, local morphology

1 | INTRODUCTION

Collision of particles and between particles and walls (or blocks) is encountered in various natural and industrial problems, such as granular flows, sand dunes, and impacts of rock fragments with protective barriers,[1–15] processes of powders and grains in pharmaceutical, chemical engineering, and polymer technology applications,[16–21] or applications in unconventional reservoir stimulation such as impacts of proppants with the walls of fractured rocks and particle plugging studies.[22–25] The problem of impact of solid objects has also been studied in the context of interaction of rock fragments originated by landslide with civil engineering structures (such as bridges) as these collisions may influence the

stability of engineering systems.[26] Thus, the multi-scale problem of collision between solid objects has attracted significant amount of inter-disciplinary research both experimentally,[27–33] analytically[34–38], and numerically using finite element methods[17,39–40] as well as discrete element methods and computational fluid dynamics techniques.[33,41–47]

There have been reported different experimental approaches in the analysis of impact mechanics problems, for example, analysing wave propagation through solids, which originates from the development of the split Hopkinson bar.[48] This technique has been widely applied in deep rock mechanics and petroleum geomechanics problems, for example in the analysis of the dynamic constitutive behavior of rocks or the examination of induced seismicity.[49–51] Even though there is a distinction in the literature, based on the velocity at impact, between low and high velocity (i.e., ballistic) collision problems, many applications, such as petroleum geomechanics and rockfall/landslide problems are examined as low-velocity (velocities are generally smaller than 10 m/s) and intermediate-velocity problems (velocities are generally between 10 and 50 m/s). In experimental impact mechanics of particle-wall (or impactor-block) systems and considering low-velocity (and intermediate-velocity) impacts, it is common to quantify from laboratory tests the coefficient of restitution (COR) which, in the case of spherical impactors colliding plane blocks, refers to the normal COR. This property is measured based on the rebound height of the impactor and in the case of perfectly elastic impacts it always corresponds to unity. In practice however the COR values are often less than unity, which implies elastoplastic response and energy dissipation,[20,52–54] commonly because of the damage on the surface of the impactor and/or the block. Factors such as the surface morphology of the impactors, for example their micro-scale roughness,[31] the type of the solid block,[32] or the presence of humidity or fluids (i.e., impactor-fluid-block systems), often termed as "wet impacts[54–59]" also influence the values of COR and attempts have been made by various researchers to examine the different influencing factors on the collision behavior of impacting bodies.

COR values are also used as input parameter in the calibration of DEM models (or coupled DEM with computational fluid dynamics codes), which can be particularly useful in the analysis of debris flows, mudflows, and other geological engineering problems.[60–65] However, apart from the interest of COR in the study of macroscopic problems, understanding the collision behavior of impactor-block systems is very useful within a contact mechanics context to understand both the behavior of two bodies in contact and also how the force chain networks develop within the block.[60,66–70]

Important insights into the collision behavior of impactor–block systems were obtained in the study by Aryaei et al.[17] combining grain-scale experiments and FEM simulations using hard (steel) and soft-ductile (aluminium) spheres colliding on the surfaces of steel sheets. One of the outcomes from their study was that the increase in impactor's diameter leads to a decrease in COR values, which was hypothesized to be caused by increased damage–plastic deformation during the collision. A parametric experimental study on the collision problem carried out by Marinack et al.[29] using a range of material types showed a significant variation in the COR values depending on the impactor and block type with the experiments involving glass beads impacting glass block or steel block to have very high COR values of the order of 0.88 to 0.95. However, values as low as 0.34-0.40 were obtained for impacts of aluminium spheres on steel blocks. The important influence of block (or the impactor) type in the COR values was also reported by Sandeep et al.,[32] in which study, hard steel and granitic blocks were used as well as softer brass blocks along with very soft rubber-type blocks. In that study, a wide range of COR values was obtained from almost elastic rebounds for glass beads or chrome steel balls impacting on granitic blocks (values slightly less than unity) to values as low as 0.40 for impacts on rubber blocks.

Despite the significant amount of research being conducted on the collision behavior of grain (or impactor) against block systems, most studies have involved engineered materials (e.g., steel, aluminium, brass, glass, rubber). In many practical applications, porous materials may be involved corresponding, for example, to soft rocks being subjected to impacts from particles, or, in many in-situ cases, the impactors may have rough textures or shape which deviates from the perfect sphere. Despite the recent insights provided in the study by Sandeep et al.[31] on the influence of surface roughness on the collision behavior of impactor-block systems, it is possible that there may be encountered competitive mechanisms in the resultant COR, for example roughness of the impactors may have different contributing mechanisms when they impact with blocks of crystalline or porous structure. Thus, in the present study it was attempted to provide some insights into the collision behavior of impactors using a wide range of impactor types against two base blocks; a soft and porous block composed of plaster simulating an analog mudrock, and a hard and crystalline block composed of polished granitic rock. The impactors had different textures (local morphologies) and also different shapes (global morphologies) and in some of the experiments the presence of fluid was also encountered to study parametrically the relative influences of different factors on the collision behavior of impactor-block systems. The range of impact velocities considered in the present experiments are 1.74 to 2.42 m/s, which are more applicable to the interaction of proppants with the walls of fractured rock. The results from the experimental impact tests, apart from their contribution to understand the collision behavior of impactor-block systems, were also utilized to calibrate a discrete-based numerical model, which further enhanced the

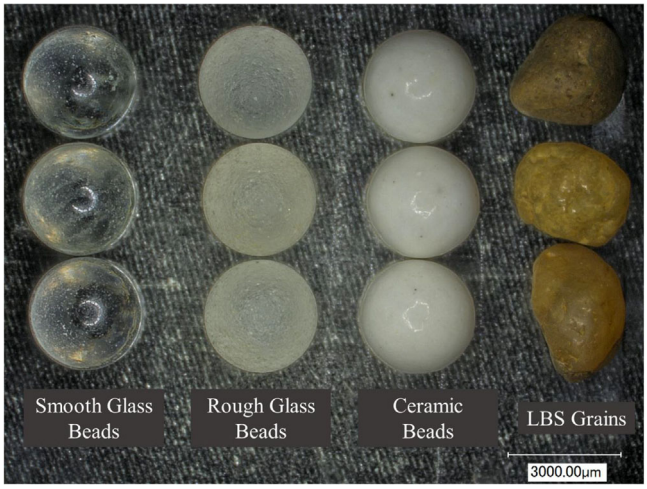

FIGURE 1 Four classes of particles (impactors) used in the collision experiments

discussions on the collision behavior of impactors on different types of blocks, thus providing a multi-scale study from experiment to numerical modelling.

2 | MATERIALS AND METHODS

2.1 | Materials

The COR of three-dimensional impacts for particle-block systems was investigated experimentally in this study and based on the laboratory test results, it was further attempted to provide additional insights on the collision behavior of particle-block (or impactor-block) systems by performing discrete-based numerical simulations. Attempting to include a range of materials in terms of properties of the particles as well as materials which are encountered as proppants in hydraulic fracturing,[71–72] the test particles included commercially available glass beads (GB-S) and ceramic beads (CB) of 3 ± 0.03 mm in diameter, as well as Leighton Buzzard sand (LBS) particles of 2.36-5.00 mm fraction. The glass and ceramic beads used in this research are perfectly spherical with relatively smooth surfaces, with RMS roughness (S_q) equal to 0.18 ± 0.05 μm (smooth glass beads) and 0.29 ± 0.13 μm (ceramic balls) based on measurements with an interferometer on a set of samples from each material type. The LBS grains have sub-rounded to rounded shape and comparatively rougher texture (S_q = 0.381 ± 0.11 μm based on a representative sample of particles used in the impact tests).

To investigate the impact behavior of rough and perfectly spherical particles, the original smooth surfaces of the glass beads were fabricated using abrasive papers so that the glass beads develop a rough surface (GB-R) while retaining their spherical shape. A standard procedure was developed, for rubbing the glass beads to consistently impose similar roughness on each particle, in which case a set of 15–20 glass beads were placed between two abrasive sheets (CW100) under a vertical confinement of 1 N weight and rotated in an orbital motion at 300 rpm for about 4 h using an orbital shaker (note that the orbital shaker has been presented in the recent studies by Kasyap and Senetakis[73] and Luo et al.,[74] predominantly in the development of artificial coatings of sand grains used in tribological and impact studies). This fabrication process resulted in S_q values of 0.47 ± 0.15 μm for the rough glass beads (2.6 times higher roughness, on average, than the smooth glass beads) so that LBS and rough glass beads had relatively similar in magnitude roughness and their major difference becomes the global shape. Subsequently, the ranges of particles tested in this study (Figure 1) covers different global (shape) and local (roughness) morphological conditions; (i) smooth and spherical (GB-S and CB), (ii) rough and spherical (GB-R), and (iii) rough and sub-rounded (LBS). Representative scanning electron microscope (SEM) images and surface profiles (obtained from white light interferometry) of these materials are shown in Figure 2. Despite the relatively lower average surface roughness (S_q) of CB and GB-S, some inherent surface damages were observed (mostly due to the packing of the grains during the surface fabrication) but the size of these microcracks was smaller than 17 μm in diameter as observed from the SEM images and surface profiles.

It should be noted that the impact behavior and final COR value would be influenced by both the local morphology (roughness) and the global morphology of the LBS grains.[31–32] However, it is technically difficult to quantify the global

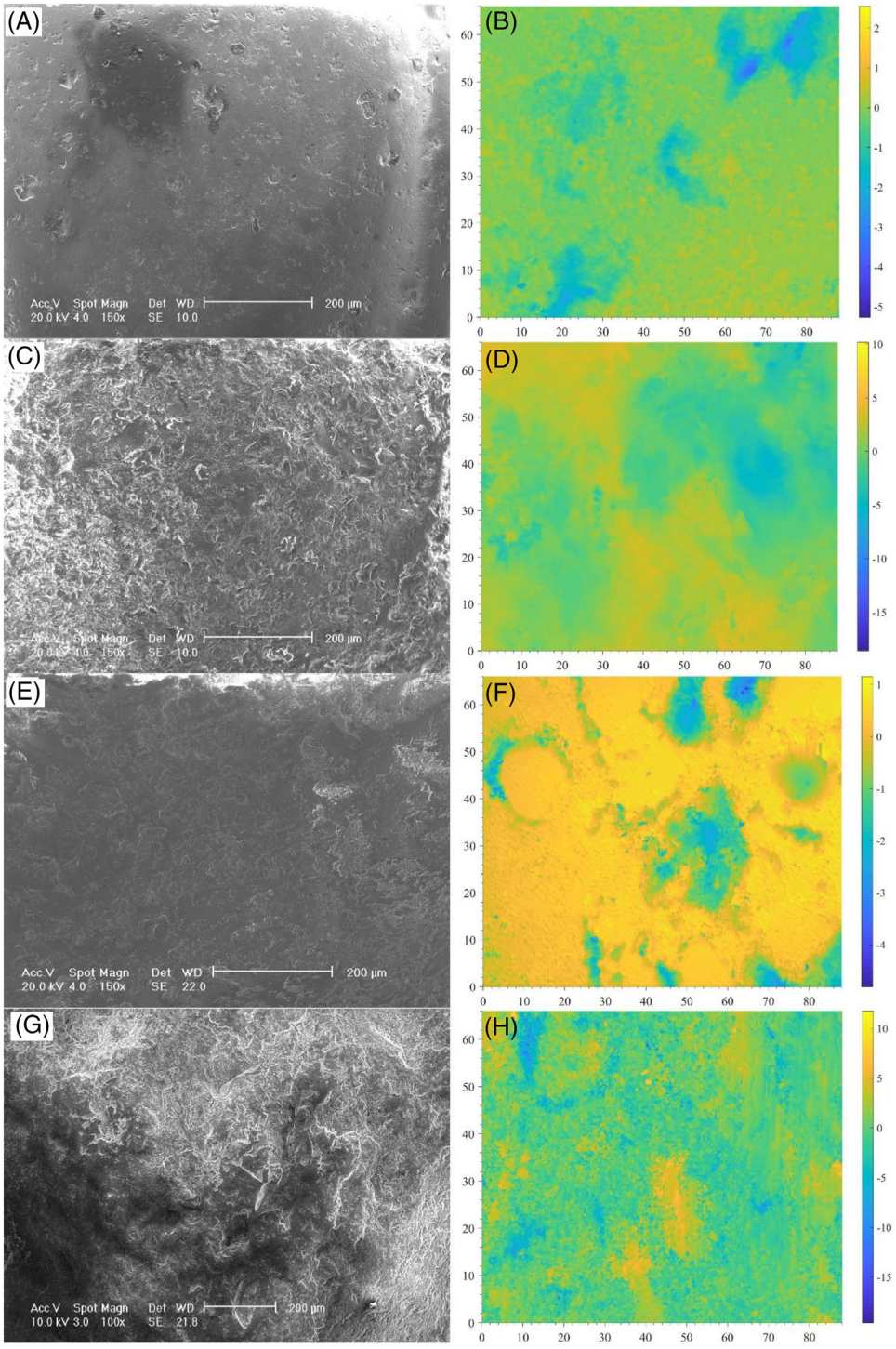

FIGURE 2 SEM images and surface profiles of (A)-(B) smooth glass beads, (C)-(D) rough glass beads, (E)-(F) ceramic beads, and (G)-(H) LBS grains

scale morphology of the particle during the impact (i.e., the exact shape of the natural grains in the vicinity of their contact with the base block). To avoid the complications in calculating the morphology of the LBS grains, particularly during the impact process, grains with high sphericity (≥0.9) and roundness (≥0.8) were carefully selected for testing. In this case, sphericity and roundness were quantified based on Krumbein and Sloss[75] empirical chart for the sample selection and careful visual observations of the particles through an optical microscope. Despite the careful selection of highly regular LBS grains, deviations in impact paths were observed and a slightly different procedure for the COR calculation was

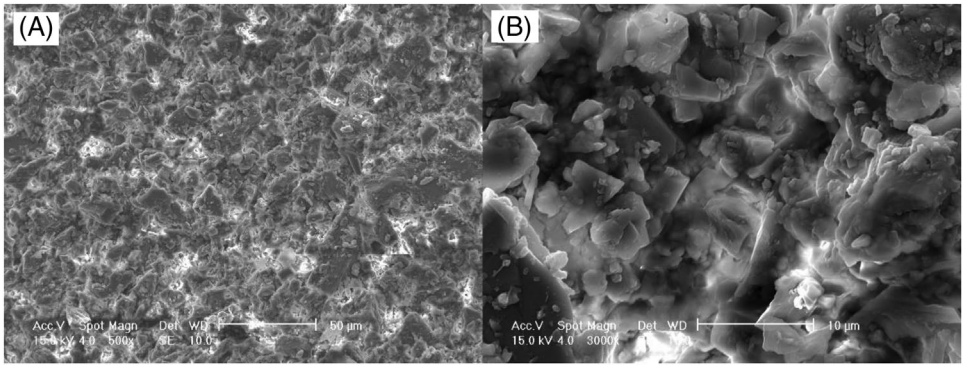

FIGURE 3 SEM images of plaster block at different magnifications (A) 500X (B) 3000X

applied for the natural grains compared to the "simpler" calculations in glass and ceramic beads, as explained in the following sections (similar to ther study by Sandeep et al[32]).

A hard, elastic block composed of polished granite and a soft, porous block composed of plaster were used as the base blocks in this study. The granitic block was of 150 × 150 mm square and 75 mm thick, while the plaster block was 70 mm in diameter and 25 mm in thickness, resulting in a particle diameter to base thickness ratio (S_d/B_t) of 0.04 and 0.12, respectively. Koller and Kolsky[27] indicated that when the ratio S_d/B_t has a magnitude smaller than 0.15, the COR value would not be affected by the plate thickness significantly and hence the influence of base thickness on COR could be considered as negligible. The granitic block was commercially procured while the plaster block was prepared in the laboratory. The plaster block was prepared with a water to plaster ratio of around 0.7, and the mixture was casted in a mold and air-dried for about 72 h. The same material was used as a bonding agent in a recent micromechanical study by Kasyap et al.,[76] while in the present work the plaster block was used as a soft-porous simulant rock (perhaps closer to a mudrock-type soft analog rock). SEM images of the plaster block (shown in Figure 3) indicated flaky particles of 2 to 20 μm in size bonded together forming an intact soft rock-like material of clastic texture.

2.2 | Methodology

2.2.1 | Experimental setup

A custom-built apparatus developed at City University of Hong Kong was used to carry out the impactor-block collision tests in this research.[31,32,74] As the impact behavior between particle and block surface with thin water layer would be analyzed in this study, some modifications were made to the laboratory configuration. Figure 4A shows the experimental setup used in this research and various parts of the apparatus. The apparatus has a plunger-solenoid system fixed on a cantilever plate, adjustable at required initial height of impact (h_I), and therefore the impact velocity (V_I), along a rigid vertical pole. This electrically operated plunger-solenoid system has two plungers moving towards and away from each other respectively to hold and release the particle (Figure 4B). This system can hold particles of diameter less than 20 mm and with a maximum holding force of 13N. Two high-speed cameras placed orthogonal to each other in the horizontal plane were used to record the impact process and therefore observing the verticality of the impact path to estimate the rebound height of the particle after impacting on the base block. Sandeep et al.[31,32] reported that in direct impacts, engineered particles such as glass beads rebound vertically following the same path as the initial drop. This was also confirmed from the experiments in the present study on smooth perfectly spherical grains (glass and ceramic beads). However, natural particles such as LBS grains slightly deviate from the initial drop path after the impact. These two cases are schematically explained in Figure 5 along with the method of calculation of heights, and hence, the corresponding COR. The calculation of COR is further discussed in Section 3.1. Even though, for oblique impacts caused by the non-spherical shape of the natural grains, would ideally necessitate the estimation of the kinetic energy before and after impact, in the present study the hypotenuse of the rebound path was used to compute the COR, a concept that has been widely applied in the analysis of the collision behavior of natural particles [Yu and Tafti,[38] Sandeep et al.,[32] Luo et al.[74]].

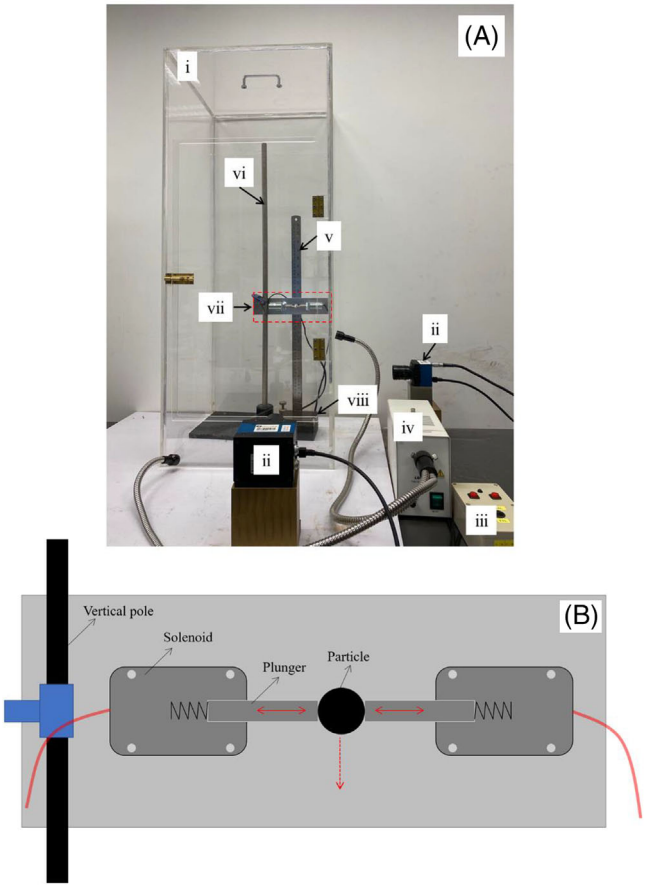

FIGURE 4 (A) Experimental setup of impact experiments with details of components (i) Perspex chamber (ii) High-speed cameras (iii) Trigger switch (iv) Focused light source (v) Scale (vi) Rigid vertical pole (vii) Solenoid-plunger system (viii) Base block (B) Schematic view of solenoid- plunger system and its functionality

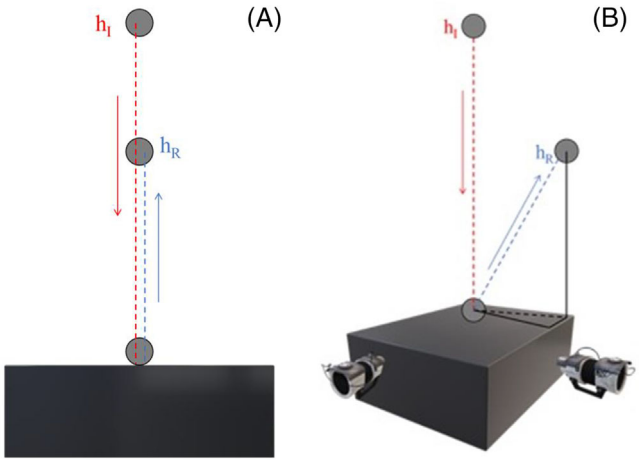

FIGURE 5 Schematic illustration of calculating rebound height and hence COR for (A) vertical rebounds and (B) oblique rebounds (red and blue dotted lines along with arrows indicate dropping and rebounding, respectively)

2.2.2 | Testing program

Impact tests were conducted with four classes of particles (GB-R, GB-S, CB, and LBS) and two classes of base blocks (granite and plaster) at four different initial drop heights (155, 190, 240, and 300 mm). These four heights correspond to impact velocities of 1.74, 1.93, 2.17, and 2.42 m/s. An additional set of experiments was conducted using granite surface

covered with a thin layer of water. Clean water (density of 997 kg/m^3) at room temperature was sprayed on the granite block surface to impose a thin fluid layer. The temperature around the apparatus was maintained at around 24 ± 0.5 °C to avoid any influence on the water layer, thus the surface of the granite accommodated water droplets which would allow studies of particle-fluid-block interactions.

Ten to fifteen tests were carried out for each combination of GB-R, GB-S, and CB particles with granite (dry and wet) and plaster blocks at four different impact velocities. Significantly low values of the coefficient of variation (CoV = ratio of absolute value of standard deviation divided by mean value) were observed in the COR values for each combination and no deviation in the rebound path was observed. For LBS grains, about thirty tests were performed for each of these combinations to assure the repeatability of the test results. In summary, a total of around 900 tests were carried out including each different group consisting of 180 tests for rough GB, smooth GB, and CB grains and 360 tests for LBS grains impacting with the three types of block surfaces (i.e., dry granite, wet granite, dry plaster) at four different collision velocities. Different grains were used for each impact test and simultaneously, the base was moved in a strategic pattern to avoid any influence of deformation incurred by the previous tests.

3 | RESULTS AND DISCUSSION

3.1 | COR

In this research, direct impact tests were conducted and so, the translational kinetic energy only in the normal direction can be used to describe the energy loss from the collision to calculate the COR. The COR between two colliding bodies is calculated from Equation (1).

$$COR = \frac{V_{R,1} - V_{R,2}}{V_{I,2} - V_{I,1}} \tag{1}$$

In Equation (1), V represents the translational velocity. The subscripts R and I represent rebound and impact phases, respectively, for the base (subscript *1*) and the impactor (subscript *2*). In the present study, the base block, is stationary throughout the impact process while the impactor is in translation. Hence, Equation (1) is simplified to Equation (2).

$$COR = -\frac{V_{R,2}}{V_{I,2}} \tag{2}$$

In Equation (2), both the velocities are vector quantities where $V_{I,2}$ is in the direction of gravity and $V_{R,2}$ is in the opposite direction, resulting in positive COR value. As discussed in Section 2, the impact and rebound velocities in this study are back-calculated from the respective heights, which are measured using high-speed cameras. Thus, the impact and rebound velocities and the corresponding COR can be calculated as shown in Equation (3).

$$COR = \frac{\sqrt{2gh_R}}{\sqrt{2gh_I}} = \sqrt{\frac{h_R}{h_I}} \tag{3}$$

In Equation (3), g represents the gravitational acceleration, h_I represents the initial drop height, and h_R is the maximum rebound height. Note that Equation (3) does not consider air drag forces, which generally would have a very small influence on the computed COR values, of the order of less than 1% based on what the literature would suggest (Marinack et al.,[29] Patil, and Higgs[19]). Equation (4) shows the COR formula if the air drag forces are considered, which is neglected in the present controlled testing.

$$COR = \left(\sqrt{\frac{g + \frac{F_{D1}}{m_s}}{g - \frac{F_{D1}}{m_s}}}\right)\left(\sqrt{\frac{h_R}{h_I}}\right) \tag{4}$$

where F_{D1} and F_{D2} are the drag forces and m_s is the mass of the sphere.

TABLE 1 COR for the impact tests of CB and smooth GB and different types of blocks

				Coefficient of Restitution values			
		Grain size		h_I(mm):155	190	240	300
Grain	Block	(mm)	Block Surface	vel(m/s):1.74	1.93	2.17	2.42
CB	Granite	3	dry	0.91 ± 0.005	0.93 ± 0.003	0.94 ± 0.004	0.95 ± 0.004
			Thin water layer	0.87 ± 0.009	0.89 ± 0.006	0.89 ± 0.006	0.9 ± 0.005
	Plaster		dry	0.29 ± 0.001	0.29 ± 0.001	0.29 ± 0.001	0.31 ± 0.000
Smooth GB	Granite		dry	0.94 ± 0.007	0.95 ± 0.007	0.95 ± 0.002	0.95 ± 0.002
			Thin water layer	0.89 ± 0.005	0.89 ± 0.004	0.91 ± 0.003	0.90 ± 0.008
	Plaster		dry	0.26 ± 0.011	0.30 ± 0.006	0.30 ± 0.005	0.29 ± 0.006

TABLE 2 COR for the impact tests of rough GB and different types of blocks

				Coefficient of Restitution values			
		Grain size		h_I(mm):155	190	240	300
Grain	Block	(mm)	Block Surface	vel(m/s):1.74	1.93	2.17	2.42
Rough GB	Granite	3	dry	0.90 ± 0.014	0.93 ± 0.015	0.93 ± 0.018	0.90 ± 0.008
			Thin water layer	0.90 ± 0.005	0.89 ± 0.009	0.87 ± 0.004	0.87 ± 0.014
	Plaster		dry	0.28 ± 0.008	0.32 ± 0.007	0.32 ± 0.006	0.31 ± 0.010

TABLE 3 COR for the impact tests of LBS and different types of blocks

				Coefficient of Restitution values			
		Grain size		h_I(mm):155	190	240	300
Grain	Block	(mm)	Block Surface	vel(m/s):1.74	1.93	2.17	2.42
LBS	Granite	3	dry	0.8 ± 0.034	0.81 ± 0.044	0.82 ± 0.029	0.82 ± 0.027
			Thin water layer	0.83 ± 0.025	0.83 ± 0.031	0.83 ± 0.046	0.83 ± 0.041
	Plaster		dry	0.26 ± 0.002	0.24 ± 0.002	0.24 ± 0.001	0.23 ± 0.000

For natural sand grains, such as LBS used in this research, the rebound path would deviate from the vertical dropping trajectory due to morphological variabilities. Therefore, for the natural particles, the rebound height can be considered as the hypotenuse (after Banks et al.[77]) calculated from the vertical and horizontal deviations of the particle away from the impact location (also shown in Figure 5B), obtained from the two orthogonally positioned high-speed cameras (Figure 4).

3.2 | Experimental simulations

Impact tests (termed as the "experimental simulations" herein) were conducted to determine the COR values for impactors with different local morphologies (roughness) and global morphologies (bulk shape) colliding hard granite (at dry and wet conditions) and soft plaster (at dry conditions) base blocks. Details of the different impactor-block combinations and the corresponding COR values at different impact velocities based on the collision experiments are listed in Tables 1–3. The tables indicate average values of COR and the corresponding standard deviation values for each group.

3.2.1 | COR of engineered particles (smooth perfectly spherical particles)

The various stages of representative tests on GB-S grains impacting on granite and plaster block surfaces are shown in Figure 6. For dry impacts, it was observed that the rebound heights and hence the COR values are significantly lower for soft plaster blocks compared to hard granite, indicating a substantial absorption of impact energy by the plaster block. This energy absorption by the plaster block was identified based on crater formation on the surface while the granite

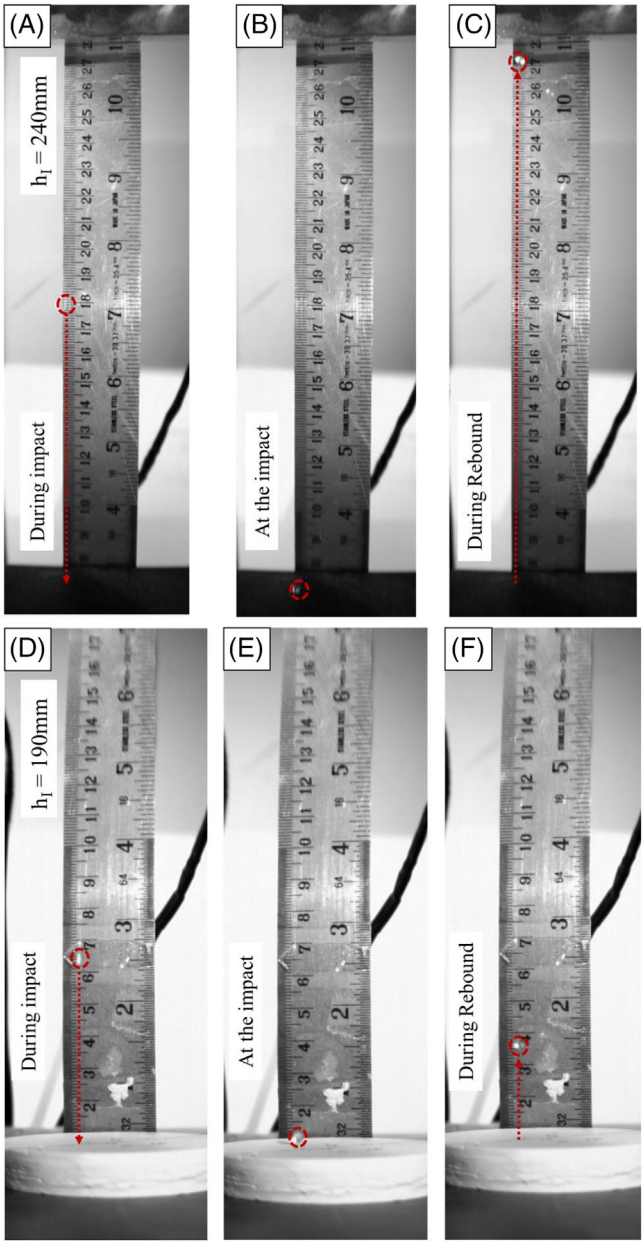

FIGURE 6 Various stages of a 3 mm glass ball impacting on granitic block and plaster block: (A) & (D) during impact (during free fall of grain) (B) & (E) at the impact (C) & (F) during rebound (rebound of grain)

block showed no damage. The collisions with dry granite surface for both GB-S and CB particles is elastoplastic with very high COR values ranging from 0.91 to 0.95. CB and GB-S showed very similar COR values at the different impact velocities. For example, at a drop height of 300 mm (V_I = 2.43 m/s), the average COR for both CB and GB-S impacting with granite was around 0.95, which was the highest value of COR among these combinations. The 5% to 10% loss in rebound velocity for these combinations of materials could be attributed to the brittle damage of micro-asperities on the glass and ceramic beads, or a minute transformation of the initial kinetic energy into translational and rotational forms which is highly challenging to resolve. As the COR is not equal to 1, that is, the yield point, it can be stated that the contact is still in elastoplastic state. Many researchers found similarly high COR values, with elastoplastic behavior for smooth engineered materials, and particularly Marinack et al.[29] found COR values of around 0.88-0.95 for glass balls impacting on "rigid" blocks of a specific type of steel and also on glass-type block. In the case of plaster base block, a significant drop in COR values was observed for both CB and GB-S particles, by around 70% compared to the granite base. Average COR values were in the range of 0.26-0.30, and these low values can be attributed to the significant damage observed on the plaster block due to the impacts. During the impact, the micro particles of the plaster block were compacted resulting in

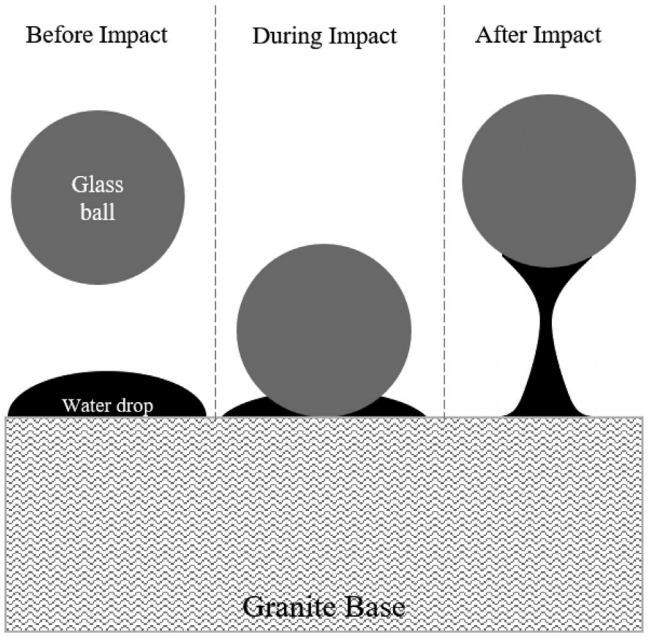

FIGURE 7 Schematic illustration of grain-fluid-block interactions and bridge formation

a significant absorption of energy and the rebound kinetic energy of the impactors is reduced. This crater formation in plaster blocks is further discussed in Section 3.2.2.

Table 1 also shows the average COR values for engineered particles impacting on hard granite block with a thin water layer (obtained by spraying water droplets on the base) at different impact velocities. The COR values reduced with thin water layer compared to the respective dry cases. GB-S and CB showed average COR values of 0.89 and 0.9 in wet case, respectively, which are only 3% to 4% lower than the dry cases. This minute decrease in COR and the corresponding additional energy loss could be attributed to the drag forces from the thin water layer. A schematic explanation shown in Figure 7 is a possible mechanism contributing to the drop in COR values. Impact tests performed by Buck et al.[59] also reported a decrease in COR values in wet impacts.

For dry collisions, the increase of the impact velocity from 1.74 to 2.42 m/s led to an increase of COR of the order of 4% for CB–granite and 1% for GB–granite. The respected coefficients of variation (CoV) were equal to 0.42% and 0.47%, respectively. Also, with the wet granite base, the variation of COR with different impact velocities was in a similar range as in the dry case, but the CoV values were slightly higher (around 0.63%) owing to the randomness in the distribution of water droplets on the granite base. In the case of plaster base with low COR values, except for the case of $V_I = 1.74$ m/s, similar COR values were observed at different impact velocities. However, slightly higher CoV values were observed, particularly with glass beads, of around 2%, owing to the highly irregular porous structure of the plaster base. A previous study by Sandeep et al.[32] found that the COR values for collisions between glass beads and granite increase with the increase in impact velocity. However, comparing the variation of COR with impact velocity and the corresponding CoV in the data, specific conclusions could not be drawn on the influence of impact velocity on the COR values, despite some general trend of slightly increasing values of COR at higher impact velocities. Hence, even for the calibration of the numerical model (discussed in Section 3.3.1), an average COR value was used for the range of velocities tested in this study.

3.2.2 | Effect of surface roughness on COR (rough perfectly spherical particles)

Table 2 shows the experimental results for rough GB grains impacting on three types of block surfaces from four different initial heights which could be compared with the results of smooth GB group to study the effect of surface roughness on the COR values. A comparison of the data in Tables 1 and 2 shows that the COR values for rough glass beads are lower than the corresponding smooth particles, by about 2% to 5% for dry and wet granite base conditions, with some exceptions at low impact velocities though. Sandeep et al.[31] also reported a small drop in the COR values when the surface roughness of the impactors increases in the case of GB impacting brass and granite block as there is an additional energy loss mechanism for rough impactors caused by the plastic deformations of surface micro-asperities. This mechanism, which has also been

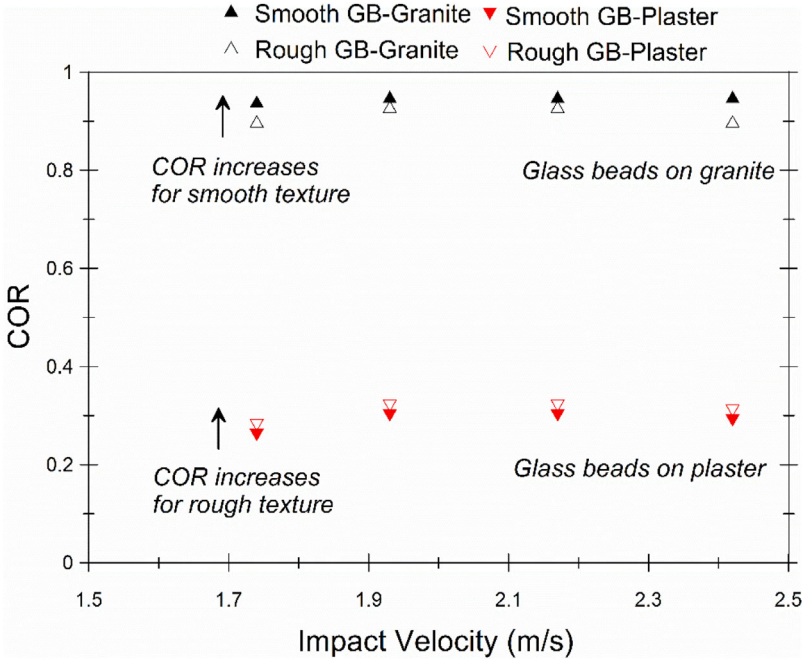

FIGURE 8 Variation of coefficient of restitution against impact velocity for smooth GB and rough GB on granite and plaster blocks

reported in "static-type" tests, is possible to be accompanied by some brittle damage of small asperities[78] of the glass beads. However, in the case of plaster block, a steady increase in COR values of about 7% to 8% was observed with rough glass beads compared to smooth glass beads, indicating a decreased energy dissipation; despite the relatively small change in COR from smooth to rough impactors (of a given type), the influence of roughness when the impactors collide with hard and soft blocks follows an opposite trend. Figure 8 shows the COR values against impact velocity for GB-S and GB-R on different blocks, illustrating the reversed trends in COR with rough and smooth glass beads with hard granite and soft plaster.

Based on the dimensions of craters formed on the plaster blocks due to impact (also discussed in Section 3.2.1) from smooth and rough glass beads, an attempt was made to explore the involved impact mechanisms. A representative set of tests at an impact velocity of 2.42 m/s was used to investigate the crater dimensions using two-dimensional contour maps of the surface obtained from a digital microscope. Figure 9 shows the 2-D contour maps of the crater at two magnifications for both rough and smooth glass bead impacts. The depth of the crater varied significantly for each case between 18.5-28.8μm and the diameter of the crater was around 450–475μm for both rough and smooth glass beads, and hence no quantitative conclusions could be drawn for these measurements. However, the 2-D contour maps in Figure 9 show distinctive differences between the rough and smooth glass bead impacts in terms of uniformity of the crater formation. For rough glass beads (Figure 9C-D), the crater formation was uniformly circular while the smooth glass beads often (Figure 9A-B) resulted in asymmetric craters. These asymmetric craters could be caused by the slipping of the glass bead on the plaster surface or from the development of rotational kinetic energy, but the quantification (or de-coupling) of these two phenomena is highly challenging at such low rebound heights. Hence, a qualitative conclusion can be made that for rough glass beads, possible partial interlocking of asperities of the glass beads with the porous structure of the plaster block resulted in lower dissipation of energy, while slipping or spinning of smooth glass beads is highly possible as evident from the asymmetric crater formation.

Another key influence of surface roughness in the impact tests was observed in the variation of COR values with repetitions based on the CoV. As discussed in the previous section, the CoV values for CB and GB-S particles ranged between 0.3% and 2% (higher for plaster than granite). In the case of rough glass beads (GB-R), the CoV values varied more consistently than smooth glass beads and the values ranged between 0.5% and 3.2%. Particularly with dry granite base, the CoV values increased from 0.5% for smooth GB case to 1.5% for rough GB case, owing to the randomness in the larger surface asperities with rough glass beads. Similar to the smooth glass bead case in Section 3.2.1, no consistent trend in the variation of COR with impact velocity could be observed owing to the scale of variation in the data with repetitions.

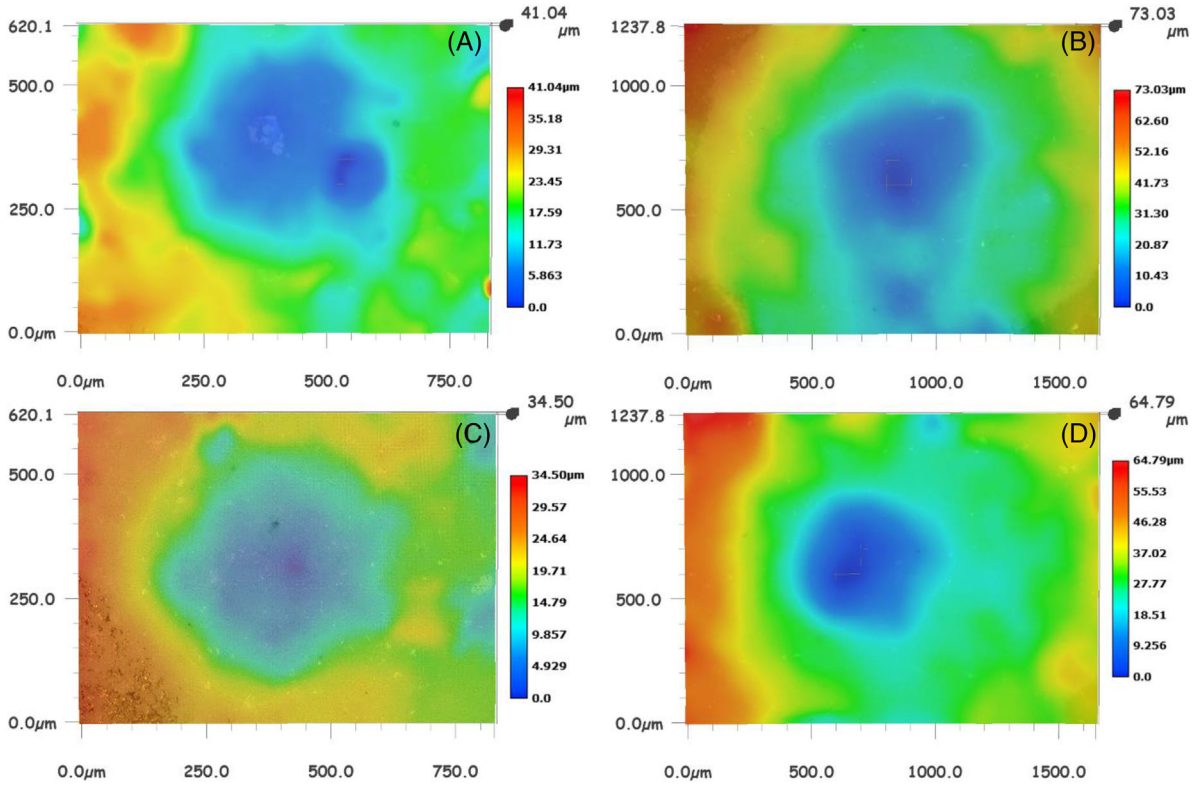

FIGURE 9 Contours of crater formed on the plaster block after impacting with (A)-(B) smooth GB and (C)-(D) rough GB (impact velocity: 2.42 m/s). The legend in each sub-figure indicates the vertical dimension of the crater with 0.0μm indicating the deepest point captured

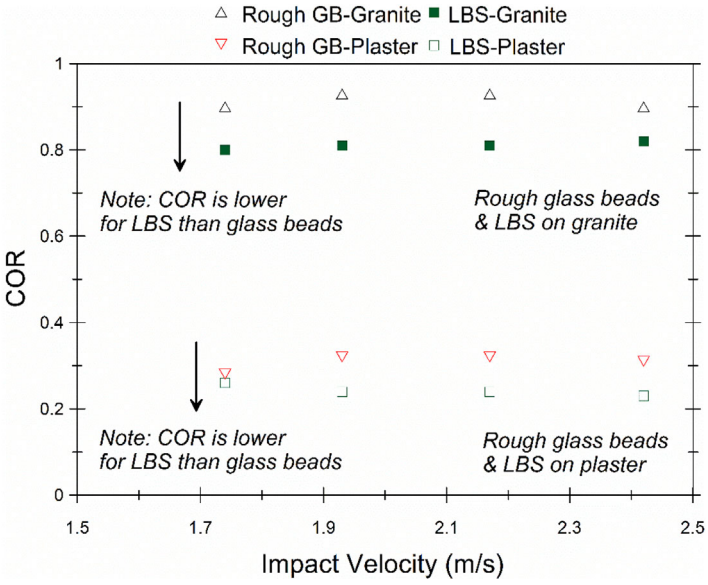

FIGURE 10 Variation of coefficient of restitution against impact velocity for LBS and rough GB on granite and plaster blocks

3.2.3 | Coefficient of restitution for natural LBS particles

The experimental results from the LBS collision tests on granite and plaster are summarized in Table 3 and Figures 10–11. The results in Figure 10 show that for both types of blocks, LBS grains result in lower values of COR compared with rough glass beads. Considering that rough glass beads and LBS grains have relatively similar local morphology in terms of RMS roughness, the data in Figure 10 would suggest that the global morphology of the LBS grains contributes to the reduction

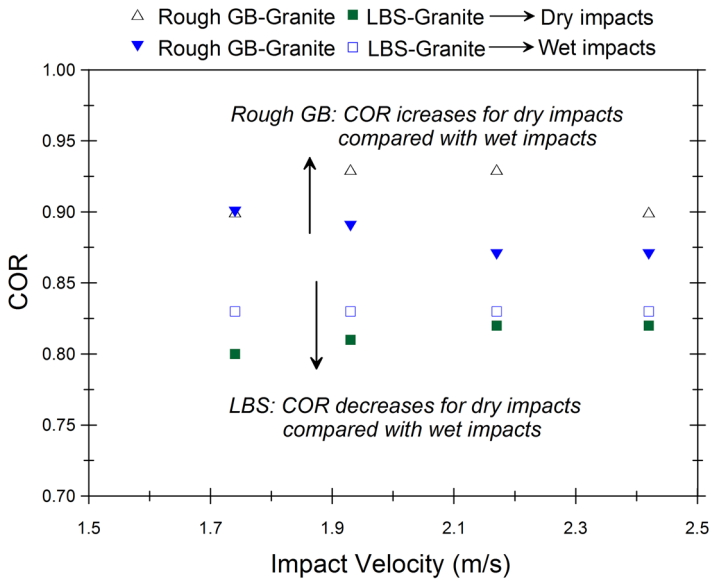

FIGURE 11 Variation of coefficient of restitution against impact velocity for LBS and rough GB on granite block in dry and wet conditions

of COR, most likely through the reduction of the translational energy introduced by some rotation of the natural particles due to the collision.

Figure 11 shows the coefficient of restitution against impact velocity for LBS and rough GB on granitic rock dry surface and granitic rock surface with thin water layer. As discussed in 3.2.1, impacting on the hard granite block with thin water layer, lower values of COR were found for smooth GB (average COR = 0.89) compared with the dry impacts. The decrease in COR values and the additional energy loss was caused by capillary forces from the thin water layer. Capillary bridge would form and rapture dissipating part of the kinetic energy of the impactors at the stage of rebound. Contrary to the impacts between GB and granite surface, in the case of LBS impacting on granite block, it is showed that the COR values increased when thin water layer was involved. For natural grains such as LBS, on one hand, shape irregularity of LBS probably prevented the formation of capillary bridge. In this way, a part of energy loss caused by the capillary force could be prevented. On the other hand, the thin water layer could buffer the energy of the impactor at the initial stage and prevent additional surface damage caused by the nonregular shape of the LBS grains. Therefore, the COR values of LBS increased in the case of impacts on granite surface with thin water layer compared to the dry case. These results suggest that while surface roughness is important in the collision behavior of impactor-block systems, the influence of thin water layer on the COR values depends on the coupled effect of both surface roughness and global morphology of the impactors, in which case the global morphology of the natural grains (i.e., deviating from being perfect spheres) seems to take over greater weight as influencing factor in the resultant COR values (note: this statement is true as long as glass beads and LBS have very similar magnitudes of RSM roughness).

3.3 | Numerical simulations

Based on the experimental results of impactors with different local and global morphologies impacting hard and soft base blocks, two extreme cases of COR values were considered for some preliminary numerical simulations. Smooth glass beads impacting hard granite and soft plaster showed extremely different COR values of about 0.95 and 0.30, respectively (around 3.2 times difference). Particle Flow Code (PFC), a commercially available discrete element modeling tool, was used to perform 2D numerical simulations of smooth glass beads impacting granite and plaster blocks. Given that the impact experiments with glass balls had perfect rebound paths, only 2D simulations were performed. Moreover, the computational cost for the impact simulations and associated calibrations would be significantly higher for 3D numerical analyses, thus the problem can be approximated in 2D.

TABLE 4 Parameters applied for impact simulations

Micro-scale parameters of the base block			
Property description		**Granite**	**Plaster**
Particles (balls)	Ball radius (mm)	1.17-2.34 (average: 1.755)	0.24-0.36 (average: 0.30)
	Normal to shear stiffness ratio	3.0	1.4
	Coefficient of friction	0.5	0.35
	Density (kg/m^3)	2750	2400
	Young's modulus (GPa)	69.7	7.9
Parallel bond	Young's modulus (GPa)		
	Normal strength (MPa)	167	32.1
	Shear strength (MPa)	167	226
	Normal to shear stiffness ratio	3.0	1.4
Properties of the impactor (glass ball)			
Bulk	Density (kg/m^3)	2600	
	Ball radius (mm)	87.75	15
	Impact velocity (m/s)	10–0.00001	
Contact with base	Model	Hertz	
	Effective shear modulus (GPa)	27.7	12.4
	Normal critical damping ratio*	0.25	0.75
	Poisson ratio	0.25	0.25

*After calibration with impact experiments.

3.3.1 | Model setup and calibrations

The bonded particle model was applied to simulate the granite and plaster blocks, and the corresponding micro-scale parameters for the model setup were derived from literature sources. Ding et al.[79] carried out PFC simulations in order to investigate the influence of model scale and particle size distribution on the simulation results using granite rock as example. The calibrated model micro-scale parameters from that work were implemented in the present study to simulate a granite rock base. Similarly, Yang et al.[80] performed PFC simulations exploring the deformation and damage behavior of mudstone specimens, where the micro-scale parameters were calibrated with respect to experimental macroscopic results. Model parameters from these two studies were adopted as shown in Table 4, with different block sizes for plaster and granite. These calibration values are however not unique and are just a result of a calibration process based on mechanical properties of the rocks (different from impact testing). Hence, additional calibration will be required for the model to reproduce the impact experimental results for a given case (i.e., combination of impactor and block types). Based on the abovementioned discussions, an average COR value of 0.95 for granite and 0.30 for plaster were targeted for an impact velocity of 1.74 m/s. The model was calibrated for targeted COR by modifying the normal critical damping ratio for the contact between the impactor (glass bead) and the base block. The dimensions of both the impactor and base block were so chosen such that the impactor radius is 50 times the average size of the base block particles and the base block dimensions are 10 times greater than the diameter of the impactor. The ratio of the block dimension to the impactor diameter was chosen based on the study of Bourrier et al.,[81] where a ratio of nine was found to be sufficient. On the other hand, the ratio of the average particle diameter (of the base) to the impactor diameter was arbitrarily chosen to have sufficient amount of contacts between them, at least in the range of velocities tested in the experiments. However, a parametric study is required to understand the influence of these ratios, which could be a potential future study recommendation. Based on the micro-scale parameters of granite and plaster blocks, the size of the impactor is 87.75 and 15 mm, while the block dimensions are 0.9 × 0.45 m and 0.15 × 0.075 m, respectively. The contact properties between the impactor and the base block for both granite and plaster are shown in Table 4.

The normal critical damping ratio (ratio of damping constant to the critical damping constant) for the Hertz contact between the impactor and the base was varied between 0 and 1 and the corresponding variation in the COR was recorded (calculated as the ratio of rebound velocity to impact velocity) to develop a calibration curve. The dashpot

energy dissipated during the contact between the bodies depends on the dashpot force (normal direction) which in turn depends on the normal critical damping ratio. Due to the softer material properties for plaster compared to granite, the COR values of glass-plaster system were extremely lower than glass-granite system at 1.74 m/s of impact velocity. In these impact simulations, the arrangement of the bonded grains in the base block significantly affected the numerical results, as the number of bonded grains in contact with the impactor during the collision and the arrangement of these bonded grains at the impact location (particularly at the surface level) change with different blocks generated in the model. In these impact simulations, different random arrangements of the bonded grains in the base block showed significantly different results, particularly in terms of number of contacts between the impactor and the base block. For a given random arrangement of the bonded grains, the orientation of the balls particularly at the surface level is unique. When the impactor contacts the base block, a different number of bonded grains interacts with the impactor depending on the velocity at collision. The specific arrangement of these bonded grains within the contact region governs the impact angle (at local scale) and hence the corresponding rebound characteristics. The influence of this bonded grain arrangement when the impactor contacts with a single grain are schematically explained is supplementary Figure S1. Depending on the microparameters of the block and the impact energy, the energy dissipation also changes with the local morphology of the bonded grains. This is particularly explained based on the change of COR values with five different cases of randomly generated base blocks at an impact velocity of 1.74 m/s, and the respective results are shown in Figure 12(A). At the calibrated impact velocity of 1.74 m/s, the number of Hertz contacts in five random simulations (i.e., between the impactor and the base block) were around 6 to 9 for granite and 11 to 13 for plaster, and hence a little deviation in the rebound path can be expected, which may not be resolvable in the corresponding experiments. The variation in COR values for these five repetitions was higher for plaster than granite. However, the simulation which showed the nearest possible value to the experimental results and (simultaneously) the least deviation in the rebound path was considered as the final calibrated model for further simulations (for both granite and plaster). Hence, from this exercise, the final calibration values of the normal critical damping ratio for granite and plaster were 0.25 and 0.75, respectively.

3.3.2 | Influence of impact velocity

With the calibrated micro-scale parameters of the base and the contact properties of impactor and base, impact simulations were carried out for two cases, that is, glass-granite and glass-plaster, with impact velocity as high as 10.0 m/s and then by decreasing the impact velocity in an attempt to estimate the yield velocity (COR = 1). Due to the high computational costs in simulating very-low velocities (< 0.00001 m/s), the smallest impact velocity simulated was 0.00001 m/s and the corresponding COR variations with impact velocity for granite and plaster base are shown in Figure 12(B). Logarithmic function was observed to best fit the data, and the corresponding function was used to estimate the yield velocity for both glass-granite and glass-plaster combinations. The estimated yield velocities for glass-granite and glass-plaster impacts were around 2.3×10^{-8} m/s and 1.1×10^{-9} m/s, respectively, indicating that the impact velocity of glass sphere required to just initiate plastic deformation in the granite is around 20 times larger than in the plaster block. The yield velocity values estimated from the present simulations are extremely smaller than the range of values (0.006 to 0.1 m/s) reported for various materials by Stronge.[20] This difference can be attributed to the precision considered for the COR estimation. It was observed from the present simulations that the yield velocity of glass-granite impact decreases by five orders of magnitude for a change in the COR values from 0.9 to 0.999, and similar was the case for glass-plaster impacts.

It was also observed that the number of Hertz contacts decreased as the impact velocity decreased (due to the smaller contact area from the low impact kinetic energy). At impact velocities lower than 0.1 m/s, the number of contacts reduced to 1, and hence the deviation in the rebound path (observed from translational velocity in other direction which is initially zero) is solely dependent on the angle of contact between the impactor and the balls which form the surface of the base block. The COR values reported in Figure 12(B) include rebound translational kinetic energy in both vertical and horizontal directions, though the contribution of the horizontal velocity was less than 0.01% of the total kinetic energy.

As the impact velocity decreased, there was observed a significant increase in contact duration (i.e., the total amount of time from the moment of impact to full rebound of the impactor) by about 1.6-2.3 times for every one-folder decrease in impact velocity. Also, the absolute values of contact time were around 2.5 times higher for glass-granite than glass-plaster impacts despite the lower COR values for plaster, owing to the plastic deformation of the plaster block forming a crater in the impact zone (as described in Section 3.3.3). One of the possible explanations for this behavior could be the different ball

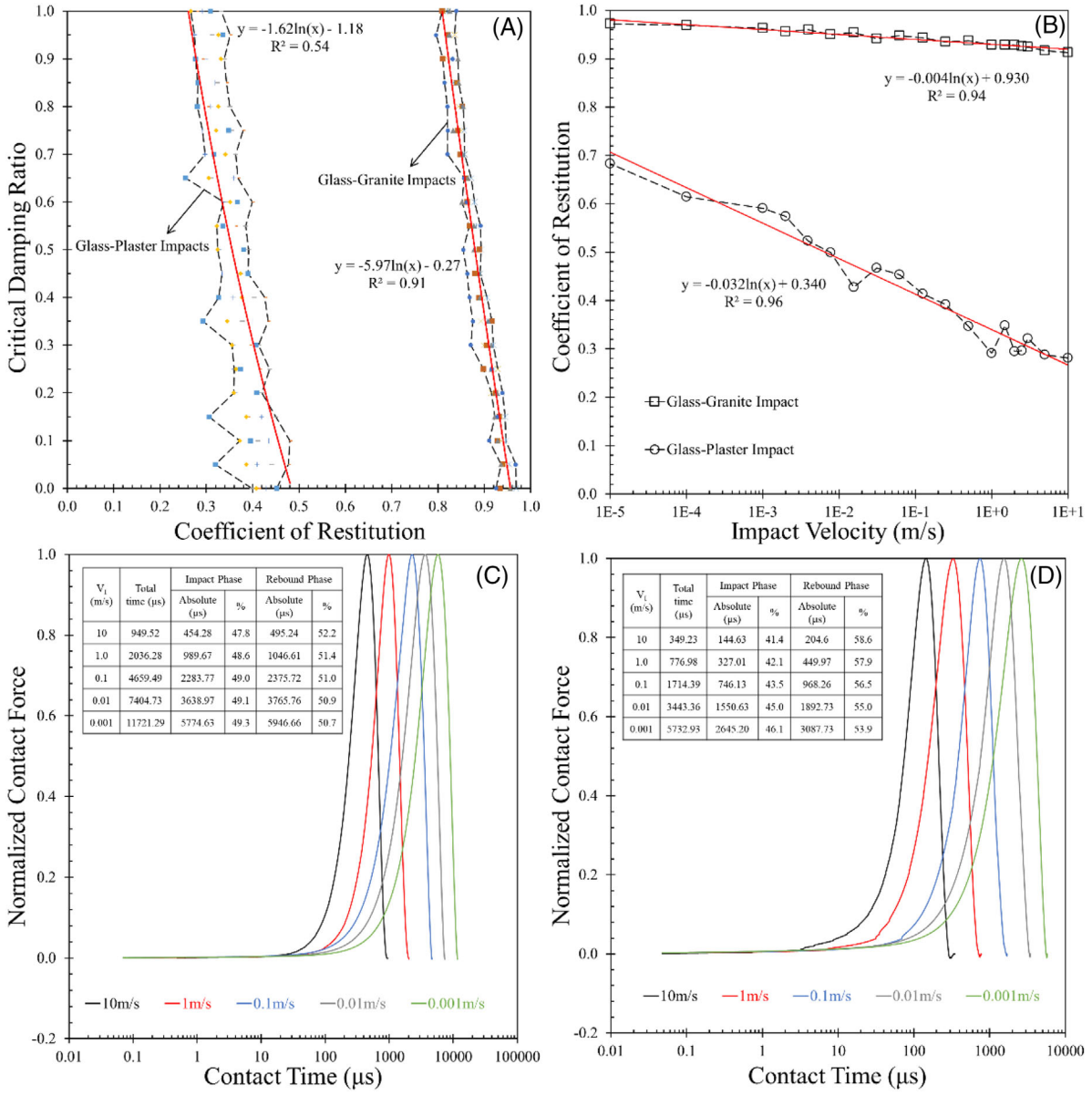

V_i (m/s)	Total time (μs)	Impact Phase		Rebound Phase	
		Absolute (μs)	%	Absolute (μs)	%
10	949.52	454.28	47.8	495.24	52.2
1.0	2036.28	989.67	48.6	1046.61	51.4
0.1	4659.49	2283.77	49.0	2375.72	51.0
0.01	7404.73	3638.97	49.1	3765.76	50.9
0.001	11721.29	5774.63	49.3	5946.66	50.7

V_i (m/s)	Total time (μs)	Impact Phase		Rebound Phase	
		Absolute (μs)	%	Absolute (μs)	%
10	349.23	144.63	41.4	204.6	58.6
1.0	776.98	327.01	42.1	449.97	57.9
0.1	1714.39	746.13	43.5	968.26	56.5
0.01	3443.36	1550.63	45.0	1892.73	55.0
0.001	5732.93	2645.20	46.1	3087.73	53.9

FIGURE 12 DEM model calibration: (A) Calibration of critical damping ratio based on experimental COR (B) Variation of numerical COR with impact velocity and corresponding logarithmic fittings (C) Influence of impact velocity on contact duration based on normalized contact force variation for glass-granite and (D) Reproduced numerical results of Fig.(C) for glass-plaster impacts

radii used for granite and plaster block models. As discussed in Section 3.3.1, the granite base model has grains larger than the plaster base model, and the internal deformations could be larger leading to larger duration of the impact process. This behavior needs to be addressed as a problem of scale effects and is beyond the scope of the present study. However, the trend of increasing contact time with decreasing impact velocity was similar for granite and plaster, and the corresponding variations are shown in Figure 12(C-D). The variation of the contact time is plotted based on the variation of the normalized contact forces (with respect to the maximum contact force) of the impactor (glass bead) for both granite and plaster base blocks at one-folder difference in impact velocities. The insets of these figures also show the numerical values of total contact time at different impact velocities and the corresponding fractions of impact and rebound phases. In both the cases of glass-granite and glass-plaster impacts, the duration of rebound phase was slightly higher than the impact phase and this difference decreased with decreasing impact velocity (i.e., approaching the yield point). The contact duration was calculated based on the time between the first and last contact of the impactor with the base. In the rebound phase, due to partial plastic deformations of the base block during the impact phase, the transformation of impact forces into rebound

kinetic energy was delayed, and this delay was higher for plaster because of its degraded mechanical properties compared with granite. These differences between granite and plaster can be observed from the inset tables in Figure 12(C-D), and the granite block results show faster approach to equal impulse (area under the force-time curve) fractions for impact and rebound phases.

3.3.3 | Behavior of base block during impact

During impact, the stresses generated from the contact of the impactor with the base propagate through the base which is one of the major contributing factors for the rebound kinetic energy of the impactor. A comprehensive understanding of the energy partitions in the whole impactor-base system, their variations with impact velocity, a qualitative interpretation of force networks for both hard granite and soft plaster models during the impact process are discoursed. Figure 13A compares the variation of kinetic energy of the impactor between the initiation and termination of the impact process as discussed in the previous section. This comparison is made with non-dimensional parameters for time and kinetic energy (ranging between 0 and 1), normalized with the respective maximum values, for a better comparison between three different impact velocities (Vi = 1, 5, and 10 m/s) and two different models (glass-granite and glass-plaster). The final datapoints of each curve give the square of COR (denoted as e^2), as described in Equation 5.

$$e^2 = \frac{KE_R}{KE_I} = \frac{1/2mV_R^2}{1/2mV_I^2} \tag{5}$$

During the impact process in a purely elastic system, the kinetic energy transferred from the impactor to the base is completely regained by the impact during the rebound phase and hence leads to a restitution coefficient of 1. In elasto-plastic systems, certain portion of the energy dissipates through the system. This dissipation happens only through the base and its contacts (within or with the impactor) as the impactor is modeled as a single rigid body in the present numerical simulations. For example, in granite-glass impact at 1 m/s ($KE_I = 31.448$J), the rebound kinetic energy (KER) was 27.439J (COR = 0.934) resulting in an energy loss of 4.009J for the impactor. A simple partition of this energy loss shows that around 99.8% is dissipated through the contacts between the balls, around 0.06% is the unrecovered strain energy in the contacts, and 0.14% is the summed up kinetic energy of the balls in the base (around 40000 balls). However, the percentage of energy dissipated through contacts slightly reduces as the impact velocity increases while the unrecovered contact strain energy and the kinetic energy of the base balls increases, in turn leading to reduced restitution coefficient (COR). Figure 13B shows the kinetic energy of the balls in the granite base after the rebound of the impactor is completed. The energy concentrations are mainly on both sides of the impact position in the vicinity of around two impactor diameters distance in the lateral direction and one impactor diameter depth into the base from the impact position as shown in Figure 13B. The energy partition details explained above apply for soft plaster base also, but the proportions change significantly as a greater portion of impactor energy loss is used in developing kinetic energy of the base balls, which can be justified from the crater formations and possible micro-cracks within the plaster base due to the impact (discussed later in this section).

The six simulation cases (three impact velocities and two base blocks) are compared for the trends of variation in the base kinetic energy (summation of kinetic energies of all balls in the base, KE_b) with the respective impact duration. Similar to Figure 13A, the impact duration is normalized for a better comparison. The KE_b values are plotted in percentages with respect to the total energy loss of the impactor in a given impact. The percent KE_b values of plaster and granite bases are plotted in two different vertical axes in Figure 13C, as they are at least two orders of magnitude different. The glass-granite impacts, which are nearly elastic (COR > 0.9 for the range of velocities tested), showed a better recovery of KE_b to its initial static condition ($KE_b = 0$), and this recovery improves as the impact velocity reduces up to the purely elastic impact condition. Also, the peak KE_b values are in the rebound phase which can be attributed to the sudden surge in the kinetic energy of the system and consequent delay in restabilizing. This skewness in the KE_b profile of glass-granite impacts gradually diminishes as the impact velocity (or the kinetic energy) reduces and the yield point (COR = 1) results in a perfectly symmetric variation with much smaller peak KEb values. In this regard, the glass-plaster impacts showed absolutely no recovery in the KEb values and the variation of the peak KE_b values is in opposite trend to the glass-granite impacts. At high velocities (10 m/s), larger crater formation and plastic damage to the base occurs in the plaster block

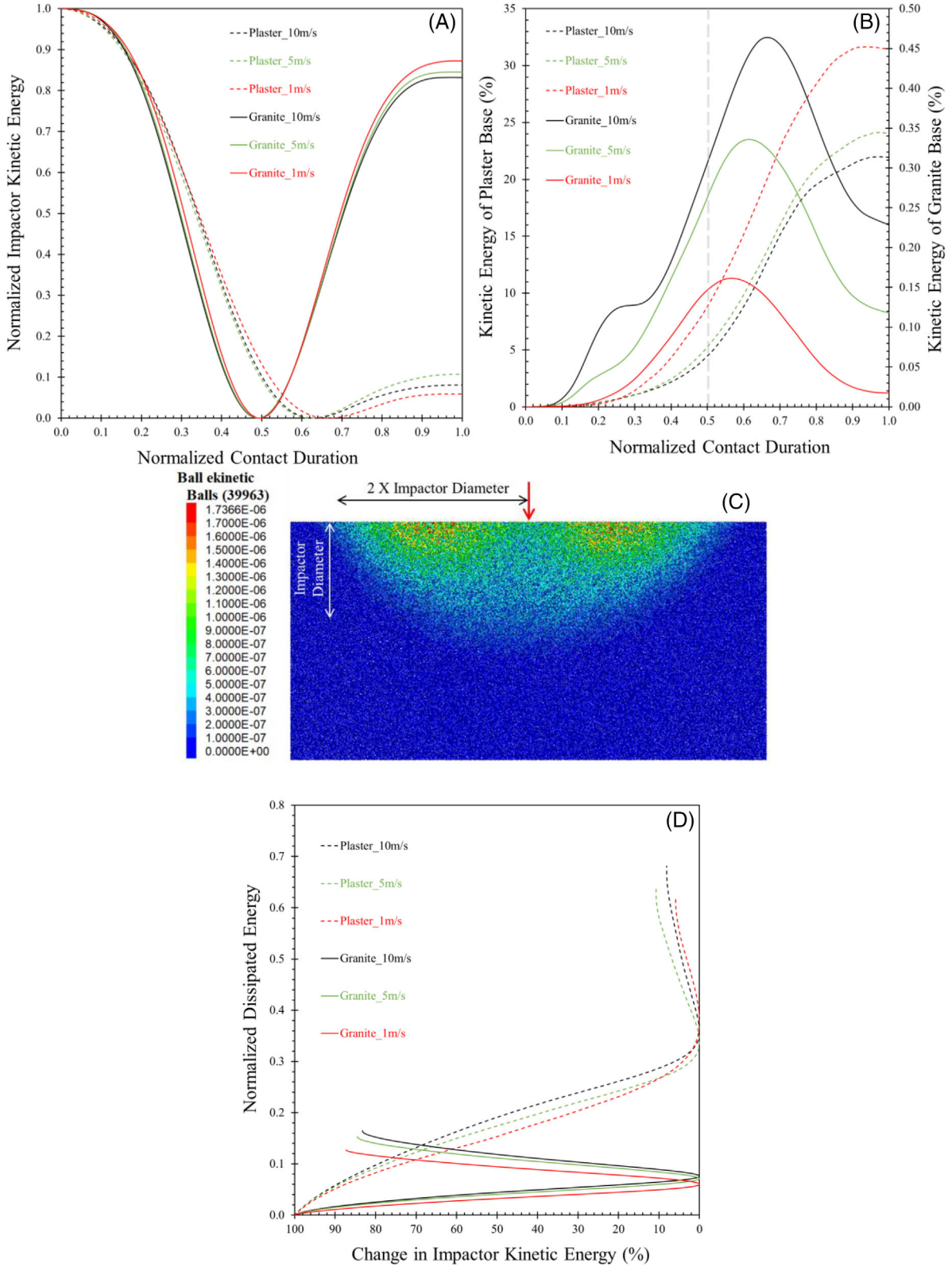

FIGURE 13 (A) Variation of impactor kinetic energy against contact duration, (B) Variation of base kinetic energy against contact duration, (C) Distribution of kinetic energy of base grains after rebound, (D) Variation of dissipated kinetic energy against change in impactor kinetic energy during the impact process. (Note: All the energy values and time durations are normalized for better comparison between plaster and granite impacts at different impact velocities)

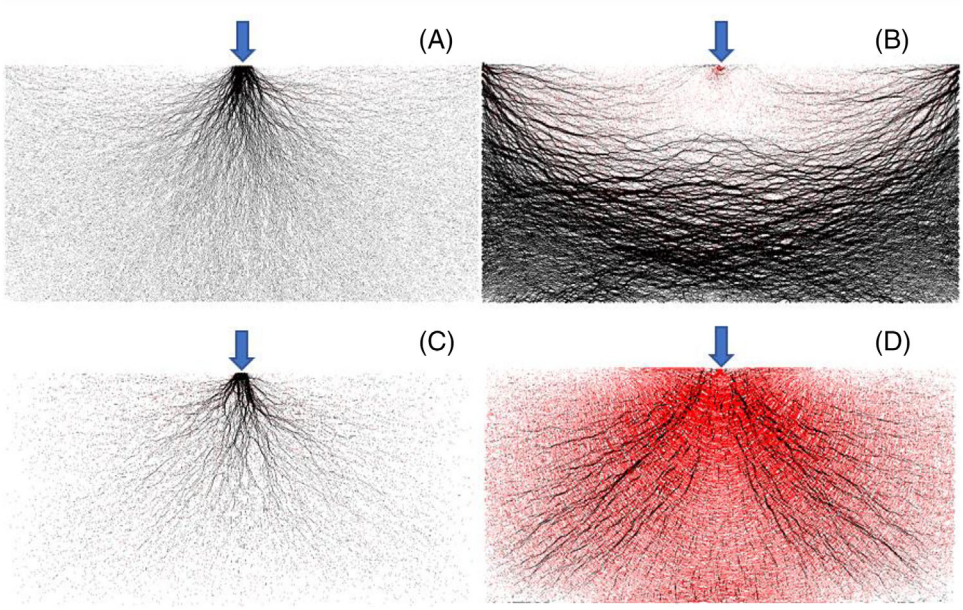

FIGURE 14 DEM results of compression and tension force chain networks in glass-granite impact simulation at the end of (A) impact phase and (B) rebound phase. Similarly for glass-plaster impact simulation at the end of (C) impact phase and (D) rebound phase. (note: red lines indicate tension, black lines indicate compression, and arrow indicates impact location)

leading to greater percentage of energy consumption in bond breakages and contact slipping and the proportion for the KE_b reduces.

Apart from the kinetic energy generated in the base, the dissipated energy from the contacts (slip energy and dashpot energy) also showed significant difference between hard granite and soft plaster and regular variation with the impact velocity. Figure 13D shows the variation of dissipated energy ratio (dissipated energy/impact kinetic energy) against the percentage change in the kinetic energy of the impactor during the impact process (0% represents the beginning of impact and 100% represents the maximum penetration point before rebound). As the impact progresses, the dissipated energy increases in both impact and rebound phases at different rates. As discussed in the previous paragraph, the quantities of dissipated energy for plaster base are significantly higher than granite base though only a slight variation with impact velocity was observed. Within this small variation, a positive correlation between dissipated energy and impact velocity was observed and the rate of increase in dissipated energy ratio was similar in both impact and rebound phases for granite base owing to the near-elastic response of the glass-granite system. However, the glass-plaster impacts showed significantly higher rate in the rebound phase than the impact phase, and the curves in Figure 13D are curvilinear, signifying more dynamic changes in the plaster base energy variation during the collision.

In the present study, qualitative observations of the compression and tension stress propagation in the base block during impact were attempted to be obtained, which provide some insights into the potential different collision mechanisms when granite or plaster block is encountered.

The force chain network for glass-granite and glass-plaster collisions at 1 m/s of impact velocity during peak contact and after rebound are shown in Figure 14. It was observed that in the granite block, compression forces dominate in the base block during the whole process of impact and the forces reorient from a radially outwards direction during the impact phase to a circumferential (tangential) direction during the rebound phase. For the soft plaster block, the impact phase is similar to granite with dominant compressive stresses propagating radially outward from the point of impact. During the rebound phase, however, the magnitude of the compressive forces reduced while the tensile forces increased. Also, the orientation of both forces did not change in the whole impact process, that is, the compression is propagated radially outwards, and the tension is circumferential. Hence, during the rebound phase, the development of circumferential tensile forces in plaster, which tend to reduce the energy transfer from the block to the impactor, explains the lower COR values compared with the granite block where the circumferential compressive forces enhance the energy transfer. The crater formation on plaster discussed in Section 3.2.2, which resulted from the compaction of the block particles and the associated macroscopic damage of the block in the vicinity of the collision area, was also observed in the simulations. The two-dimensional approximation of the crater has its limitations on the actual dimensions of the crater

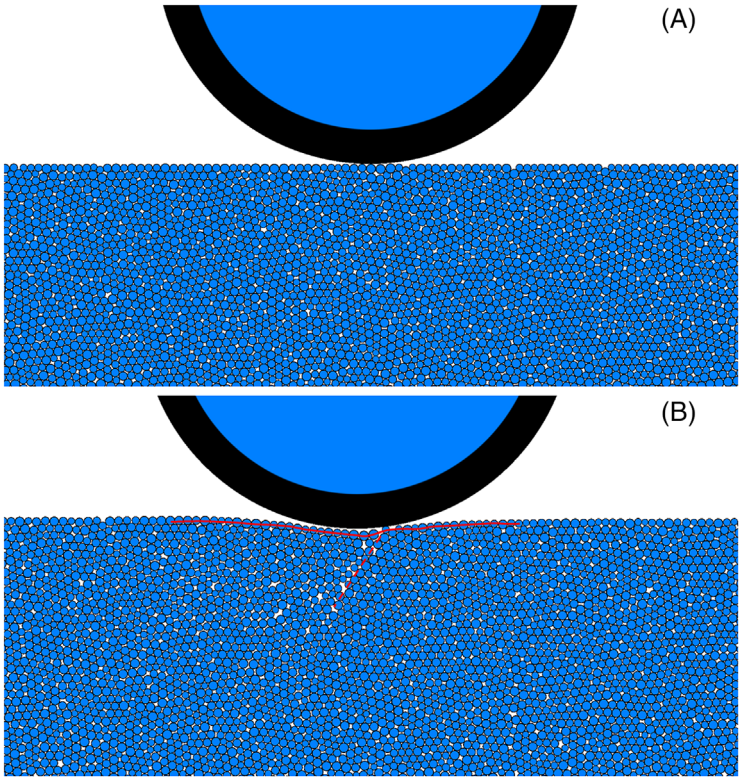

FIGURE 15 Condition of plaster base grains (A) before and (B) after impact from the DEM simulations highlighting the crater formation

(in 3D), particularly with the depth of the dimensions of the crater which are possibly over-estimated in 2D. Figure 15(A-B) shows the position of the impactor and the base before and after the impact, highlighting the crater formation in the base in two-dimensional view. The development of significant tensile forces in the rebound phase for plaster base also explains the negative contact forces on the impactor during the end of the rebound phase. As shown in Figure 14(C-D), at the end of the rebound phase, some negative contact forces (tension) were observed for both glass-granite and glass-plaster impacts. However, the magnitudes of these tensile forces are as high as 1.1% (as portion of the maximum contact force) for plaster impacts while granite showed only 0.1% to 0.3%.

4 | CONCLUSIONS

Engineered impactors of smooth glass beads (GB-S) and ceramic balls (CB) impacting on dry granitic block showed very high COR values of the order of 0.91-0.95 indicating elastoplastic behavior, which was attributed to some minute transformation of the kinetic energy to translational and rotational forms. The COR values for these impactor-block combinations slightly decreased (around 3% to 4% drop) for collisions on wet surfaces of granite. In impacts of GB-S and CB with plaster, the COR values significantly decreased to 0.26-0.30 as the collision resulted in compaction and plastic damage of the surface of the plaster block. Based on collision tests on smooth and rough glass beads (GB-S, GB-R), it was observed that the roughness had opposite influences when the impactor collided the hard granitic block and the soft plaster block. Image process was implemented to analyze the formed crater on the plaster surfaces from the impacts and the contour maps indicated similar size and depth of the craters for smooth and rough glass beads impacting on the soft-porous plaster block. For GB-R, the crater formation was uniformly circular, whereas for GB-S the craters were asymmetric indicating a possible slipping of the smooth glass beads on the plaster surface contributed by some rotational kinetic energy. This mechanism was prevented for rough glass beads impacting on plaster leading to a qualitative conclusion that partial interlocking of the small asperities of the GB-R with the porous structure of the plaster prevented the development of additional rotational kinetic energy resulting in slightly higher COR values compared to the smooth glass beads. For the natural LBS grains impacting on dry granite and plaster, the experimental results showed relatively lower COR values compared to the tests on rough glass beads leading to the conclusion that the global morphology of the impactors had comparatively a greater weighted influence than the surface roughness for dry impacts. However, the influence of thin water layer had opposite trends between glass beads–granite and LBS–granite, with the LBS grains to show increased COR values for wet impacts

compared with dry impacts. Numerical simulations were performed using the PFC2D program taking two given cases from the experiments in the calibration process: smooth glass beads impacting granite and plaster base blocks. The DEM results indicated yield velocities of the order of 2.3×10^{-8} and 1.1×10^{-9} m/s for granite and plaster blocks, respectively, leading to the conclusion that the impact velocity of glass beads required to initiate plastic deformation in the granitic block was around 20 times larger than in the plaster block. Additionally, the numerical results showed increased contact duration between impactor and block with decreasing impact velocity for both types of blocks. Quantification of the force chain networks at impact showed that at the collision, both granitic and plaster blocks developed, predominantly, compressive stresses. In granite, the stresses re-distributed from a radially outwards direction in the collision phase to a circumferential direction in the rebound phase. For plaster, the collision phase was similar to the granite, however, the (circumferential) tensile stresses increased in the rebound phase, which could provide a micromechanical-based mechanism of the reduced COR in plaster impacts.

ACKNOWLEDGMENTS

The work described in this article was fully supported by the grants from the Research Grants Council of the Hong Kong Special Administrative Region, China, project number: "CityU 11210419" and project number: "CityU 11214218".

DATA AVAILABILITY STATEMENT

The data that support the findings of this study are available from the corresponding author upon reasonable request.

ORCID

Kostas Senetakis https://orcid.org/0000-0003-0190-4768

REFERENCES

1. Iverson RM. The physics of debris flows. *Rea Geophys*. 1997;35:245-296.
2. Clelland R, Hrenya CM. Simulations of a binary-sized mixture of inelastic grains in rapid shear flow. *Phys Rev E*. 2002;65(3):031301.
3. Agliardi F, GB Crosta. High resolution three-dimensional numerical modelling of rockfalls. *Int J Rock Mech Min Sci*. 2003;40(4):455-471.
4. Di Prisco C, Vecchiotti M. A rheological model for the description of boulder impacts on granular strata. *Geotechnique*. 2006;56(7):469.
5. Turmel D, Locat J. Numerical modelling of underwater rockfalls. *Canad Geotech J*. 2010;48(1):16-25.
6. Durda DD, Movshovitz N, Richardson DC, et al. Experimental determination of the coefficient of restitution for meter-scale granite spheres. *Icarus*. 2011;211(1):849-855.
7. Asteriou P, Saroglou H, Tsiambaos G. Geotechnical and kinematic parameters affecting the coefficients of restitution for rock fall analysis. *Int J Rock Mech Min Sci*. 2012;54:103-113.
8. Choi CE, Ng CWW, Law RP, Song D, Kwan JSH, Ho KKS. Computational investigation of baffle configuration on impedance of channelized debris flow. *Canad Geotech J*. 2014;52(2):182-197.
9. Jiang S, Shen L, Guillard F, Einav I. Energy dissipation from two-glass-bead chains under impact. *Int J Impact Eng*. 2018;114:160-168.
10. Shen W, Zhao T, Dai F, Jiang M, Zhou GGD. DEM analyses of rock block shape effect on the response of rockfall impact against a soil buffering layer. *Eng Geol*. 2019;249:60-70.
11. Naito N, Maeda K, Konno H, Ushiwatari Y, Suzuki K, Kawase R. Rockfall impacts on sand cushions with different soil mechanical characteristics using discrete element method. *Soils Foundat*. 2020;60:384-397.
12. Fang J, Wang LZ, Hong Y, Zhao JD. Influence of solid-fluid interaction on impact dynamics against rigid barrier:cFD-DEM modelling. *Géotechnique*. 2021. [In Press].
13. Kong Y, Zhao JD, Li XY. Hydrodynamic dead zone in multiphase geophysical flows impacting a rigid obstacle. *Powder Technol*. 2021;386:335-349.
14. Tan DY, Feng WQ, Yin JH, Zhu ZH, Qin JQ. Numerical study of retention efficiency of a flexible barrier in mitigating granular flow comparing with large-scale physical modeling test data. *Acta Geotech*. 2021;16:433-448.
15. Yang E, Bui HH, Nguyen GD, et al. Numerical investigation of the mechanism of granular flow impact on rigid control structures. *Acta Geotech*. 2021. https://link.springer.com/article/10.1007/s11440-021-01162-4. [Published Online].
16. Kozicki J, Tejchman J. Application of a cellular automaton to simulations of granular flow in silos. *Granul Matter*. 2005;7:45-54.
17. Aryaei A, Hashemnia K, Jafarpur K. Experimental and numerical study of ball size effect on restitution coefficient in low velocity impacts. *Int J Impact Eng*. 2010;37:1037-1044.
18. Diani J, Gilormini P, Agbobada G. Experimental study and numerical simulation of the vertical bounce of a polymer ball over a wide temperature range. *J Mater Sci*. 2014;49:2154-2163.
19. Patil D, Higgs III CF. Experimental investigations on the coefficient of restitution for sphere-thin plate elastoplastic impact. *J Tribol*. 2017;140(1):011406.
20. Stronge WJ. *Impact Mechanics*. 2nd ed. Cambridge University Press; 2018.

21. Li X, Dong M, Li S, Shang Y. Experimental and theoretical studies of the relationship between dry and humid normal restitution coefficients. *J Aerosol Sci*. 2019;129:16-27.
22. Tomac I, Gutierrez M. Micromechanics of proppants agglomeration during settling in hydraulic fractures. *J Petrol Explor Produc Technol*. 2015;5:417-434.
23. Zhang Y, Lu X, Zhang X, Li P, Numerical Simulation of Proppant Transportation in Hydraulic Fracture Based on DDPM-KTGF Model. *ASME-JSME-KSME 2019 8th Joint Fluids Engineering Conference*, San Francisco, USA, 2019 https://doi.org/10.1115/AJKFluids2019-5613.
24. Huang H, Babadagli T, Li H, Develi K, Zhou D. A visual experimental study on proppants transport in rough vertical fractures. *Int J Rock Mech Min Sci*. 2020;134:104446.
25. Wang Y, Li X, Zhao B, Zhang Z. Numerical simulation of particle plugging in hydraulic fracture by element partition method. *Int J Numer Anal Methods in Geom*. 2020;44(14):1857-1879.
26. Lu YE, Zhang LM. Analysis of failure of a bridge foundation under rock impact. *Acta Geotech*. 2012;7:57-68.
27. Koller MG, Kolsky H. Waves produced by the elastic impacts of spheres on thick plates. *Int J Solids Struct*. 1987;23(10):1387-1400.
28. Lorenz A, Tuozzolo C, Louge MY. Measurements of impact properties of small, nearly spherical particles. *Exp Mech*. 1997;37(3):292-298.
29. MC Marinack Jr, Musgrave RE, Higgs III CF. Experimental investigations on the coefficient of restitution of single particles. *Tribol Trans*. 2013;56:572-580.
30. Higham JE, Shepley P, Shahnam M. Measuring the coefficient of restitution for all six degrees of freedom. *Granular Matter*. 2019;21:15.
31. Sandeep CS, Luo L, Senetakis K. Effect of grain size and surface roughness on the normal coefficient of restitution of single grains. *Materials*. 2020;814:1-13.
32. Sandeep CS, Senetakis K, Cheung DKH, et al. Experimental study on the coefficient of restitution of grain against block interfaces for natural and engineered materials. *Canad Geotech J*. 2021;58(1):35-48.
33. Wang L, Zheng Z, Yu Y, Liu T, Zhang Z. Determination of the energetic coefficient of restitution of maize grain based on laboratory experiments and DEM simulations. *Powder Technol*. 2020;362:645-658.
34. Thornton C. Coefficient of restitution for collinear collisions of elastic-perfectly plastic spheres. *J Appl Mech*. 1997;64:383-386.
35. Brach RM. Formulation of rigid body impact problems using generalized coefficients. *Int J Eng Sci*. 1998;36(1):61-71.
36. Vu-Quoc L, Zhang X, Lesburg L. A normal force-displacement model for contacting spheres accounting for plastic deformation:force-driven formulation. *J Appl Mech*. 2000;67:363-371.
37. Jackson RL, Green I, Marghitu DB. Predicting the coefficient of restitution of impacting elastic-perfectly plastic spheres. *Nonlinear Dyn*. 2010;60:217-229.
38. Yu K, Tafti D. Impact model for micrometer-sized sand particles. *Powder Technol*. 2016;294:11-21.
39. Zhang X, Vu-Quoc L. Modeling the dependence of the coefficient of restitution on the impact velocity in elasto-plastic collisions. *Int J Impact Eng*. 2002;27:317-341.
40. Coaplen J, Stronge WJ, Ravani B. Work equivalent composite coefficient of restitution. *Int J Impact Eng*. 2004;30:581-591.
41. Moriguchi S, Borja RI, Yashima A, Sawada K. Estimating the impact force generated by granular flow on a rigid obstruction. *Acta Geotech*. 2009;4:57-71.
42. Teufelsbauer H, Wang Y, Pudasaini SP, Borja RI, Wu W. DEM simulation of impact force exerted by granular flow on rigid structures. *Acta Geotech*. 2011;6:119.
43. Wang Y, Tonon F. discrete element modeling of rock fragmentation upon impact in rock fall analysis. *Rock Mech Rock Eng*. 2011;44:23-35.
44. Calvetti F, di Prisco CG, Vairaktaris E. DEM assessment of impact forces of dry granular masses on rigid barriers. *Acta Geotech*. 2017;12:129-144.
45. Shen WG, Zhao T, Zhao JD, Dai F, Zhou GD. Quantifying the impact of dry debris flow against a rigid barrier by DEM analyses. *Eng Geol*. 2018;241:86-96.
46. Jiang Z, Du J, Rieck C, Bück A, Tsotsas E. PTV experiments and DEM simulations of the coefficient of restitution for irregular particles impacting on horizontal substrates. *Powder Technol*. 2019;360:352-365.
47. Tang H, Song R, Dong Y, Song X. Measurement of restitution and friction coefficients for granular particles and discrete element simulation for the tests of glass beads. *Materials*. 2019;12(19):3170.
48. Ogawa K. Impact-tension compression test by using a split-hopkinson bar. *Exp Mech*. 1984;24:81-86.
49. Wang S, Liu Y, Du K, et al. Waveform features and failure patterns of hollow cylindrical sandstone specimens under repetitive impact and triaxial confinements. *Geomech Geophys Geo-energ Geo-resour*. 2020;6(57).
50. Wang S, Xiong X, Liu Y, et al. Stress–strain relationship of sandstone under confining pressure with repetitive impact. *Geomech Geophys Geo-Energ Geo-Resour*. 2021;7(39).
51. Li N, Zhou Y, Li H. Experimental study for the effect of joint surface characteristics on stress wave propagation. *Geomech Geophys Geo-Energ Geo-Resour*. 2021;7(50).
52. Kharaz AH, Gorham DA. A study of the restitution coefficient in elastic-plastic impact. *Philos Mag Lett*. 2000;80:549-559.
53. Seifried R, Schiehlen W, Eberhard P. Numerical and experimental evaluation of the coefficient of restitution for repeated impacts. *Int J Impact Eng*. 2005;321:508-524.
54. Chen R, Liang M, Luo J, Lei H, Guo D, Hu X. Comparison of surface damage under the dry and wet impact:molecular dynamics simulation. *Appl Surf Sci*. 2011;258(5):1756-1761.
55. Müller T, Gollwitzer F, Krülle CA, Rehberg I, Huang K. Scaling of the normal coefficient of restitution for wet impacts. *AIP Conf Proc*. 2013;1542:787.

56. Müller T, Huang K. Influence of the liquid film thickness on the coefficient of restitution for wet particles. *Phys Rev*. 2016;93:042904.
57. Crüger B, Heinrich S, Antonyuk S, Deen NG, Kuipers JAM. Experimental study of oblique impact of particles on wet surfaces. *Chem Eng Res Des*. 2016;110:209-219.
58. Crüger B, Salikov V, Heinrich S, et al. Coefficient of restitution for particles impacting on wet surfaces:an improved experimental approach. *Particuology*. 2016;25:1-9.
59. Buck B, Tang Y, Deen NG, Kuipers JAM, Heinrich S. Dynamics of wet particle-wall collisions:influence of wetting condition. *Chem Eng Res Des*. 2018;135:21-29.
60. Dahl SR, Clelland R, Hrenya CM. Three-dimensional, rapid shear flow of particles with continuous size distributions. *Powder Technol*. 2003;138(1):7-12.
61. Zhang J, Hu Z, Ge W, Zhang Y, Li T, Li J. Application of the discrete approach to the simulation of size segregation on granular chute flow. *Ind Eng Chem Res*. 2004;43:5521-5528.
62. Jasti VK, Higgs CF. A fast first order model of a rough annular shear cell using cellular automata. *Granular Matter*. 2010;12(1):97-106.
63. Cui Y, Choi CE, Lui LHD, Ng CWW. Effects of particle size of mono-disperse granular flows impacting a rigid barrier. *Nat Hazards*. 2018;91:1179-1201.
64. Li X, Zhao J. A unified CFD-DEM approach for modeling of debris flow impacts on flexible barriers. *Int J Numer Anal Methods Geomech*. 2018;42:1643-1670.
65. Ge J, Monroe CA. The effect of coefficient of restitution in modeling of sand granular flow for core making:part I Free-fall experiment and theory. *Int J Metalcast*. 2019;13:753-767.
66. Wu C, Ly Li, Thornton C. Rebound behaviour of spheres for plastic impacts. *Intl J Impact Eng*. 2003;28:929-946.
67. Schwager T, Pöschel T. Coefficient of restitution and linear–dashpot model revisited. *Granular Matter*. 2007;9:465-469.
68. Schwager T, Pöschel T. Coefficient of restitution for viscoelastic spheres:the effect of delayed recovery. *Phys Rev E*. 2007:051304.
69. Cisneros LAT, Marzulli V, Windows-Yule CRK, Pöschel T. Impact in granular matter:force at the base of a container made with one movable wall. *Phys Rev E*. 2020;102(1):012903.
70. Marzulli V, Torres Cisneros LA, di Lernia A, et al. Impact on granular bed: validation of discrete element modeling results by means of two-dimensional finite element analysis. *Granular Matter*. 2020;22(1):27.
71. Bandara KMAS, Ranjith PG, Rathnaweera TD. Extensive analysis of single ceramic proppant fracture mechanism and the influence of realistic extreme reservoir conditions on proppant mechanical performance. *J Pet Sci Eng*. 2020;195:107586.
72. Bandara KMAS, Ranjith PG, Rathnaweera TD, Wanniarachchi WAM, Yang SQ. Crushing and embedment of proppant packs under cyclic loading: an insight to enhanced unconventional oil/gas recovery. *Geoscience Frontiers*. 2020.
73. Kasyap SS, Senetakis K. A micromechanical experimental study of kaolinite-coated sand grains. *Tribol Int*. 2018;126:206-217.
74. Luo L, Ren J, Kasyap SS, Senetakis K. A note on the influence of smectite coating on the coefficient of restitution of natural sand particles impacting granitic blocks. *Coatings*. 2021;11:996.
75. Krumbein WC, Sloss LL. Stratigraphy and sedimentation. *Soil Sci*. 1951;5:401-482.
76. Kasyap SS, Senetakis K, Coop MR, Zhao J. Micromechanical behaviour in shearing of reproduced flat LBS grains with strong and weak artificial bonds. *Acta Geotech*. 2021;16(5):1355-1376.
77. Banks M, Bridges NT, Benzit M. Measurements of the coefficient of restitution of quartz sand on basalt: implications for abrasion rates on earth and mars. *Lunar Planetary Sci*. 2005:2116.
78. Sandeep CS, Li S, Senetakis K. Scale and surface morphology effects on the micromechanical contact behavior of granular materials. *Tribol Int*. 2021;159:106929.
79. Ding X, Zhang L, Zhu H, Zhang Q. Effect of model scale and particle size distribution on PFC3D simulation results. *Rock Mech Rock Eng*. 2014;47:2139-2156.
80. Yang SQ, Tian WL, Jing HW, Huang YH, Yang XX, Meng B. Deformation and damage failure behavior of mudstone specimens under single-stage and multi-stage triaxial compression. *Rock Mech Rock Eng*. 2019;52:673-689.
81. Bourrier F, Nicot F, Darve F. Physical processes within a 2D granular layer during an impact. *Granular Matter*. 2008;10(6):415-437.

SUPPORTING INFORMATION

Additional supporting information may be found in the online version of the article at the publisher's website.

How to cite this article: Luo L, Kasyap SS, He H,Senetakis K. Laboratory and discrete-based numerical investigation on the collision problem of impactor-block systems with soft-porous and hard-crystalline analog rocks. *Int J Numer Anal Methods Geomech*. 2021;1–23. https://doi.org/10.1002/nag.3313